JOURNAL OF AIRCRAFT
Vol. 45, No. 1, January–February 2008

Simultaneous Airframe and Propulsion Cycle Optimization for Supersonic Aircraft Design

Sriram K. Rallabhandi* and Dimitri N. Mavris†
Georgia Institute of Technology, Atlanta, Georgia 30332

DOI: 10.2514/1.33183

Supersonic aircraft design includes several tradeoffs, each with advantages and disadvantages. The selection of aircraft shape to meet the prescribed requirements is a nontrivial exercise in the case of commercial supersonic configurations with multiple stringent constraints. The number of discrete shape options, along with the detailed aircraft shaping, presents a difficult choice to the configuration designer. Most often, the aircraft shape is frozen, based on experience. In the case of revolutionary shapes or designs, such a choice would be suboptimal. Furthermore, unlike the subsonic designs, the propulsion cycle plays a much more important role than in the earlier stages of design in the case of supersonic configurations. This paper presents an approach for the simultaneous inclusion of airframe and propulsion system parameters in the aircraft design process. The proposed approach parameterizes the geometry in terms of several shape variables and the propulsion system in terms of representative cycle variables. Advanced genetic algorithms are developed and employed to obtain aircraft configurations and propulsion cycle parameters that simultaneously optimize several critical performance metrics including range, sonic boom loudness, and jet velocity. Results from the optimization are presented and design tradeoffs are discussed.

Nomenclature

g_m	=	goal value associated with the mth objective
M	=	number of objectives
n_m	=	normalization value associated with the mth objective
T41	=	turbine rotor inlet temperature
T41MAX	=	maximum turbine rotor inlet temperature
T41SLS	=	sea-level static turbine rotor inlet temperature
w_m	=	weight associated with the mth objective

I. Introduction

SUPERSONIC aircraft design has received renewed impetus in the recent past due to advances in aircraft shaping and other technologies. Various market studies [1,2] have concluded that there exists a significant market for a commercial supersonic business jet. Such an aircraft, if successful, would significantly reduce the trip time and pave the way for larger supersonic transports in the future. However, several bottlenecks, including regulatory ones, have to be overcome before such a design becomes reality. Because of stringent noise and performance requirements, commercial supersonic aircraft design is a challenging task. Several organizations and entities [3–5] have proposed potential designs that could meet the requirements to various degrees. These designs are obtained after several manual iterations. Because of the revolutionary nature of these designs, the design methods that rely on historical data cannot be used. Accordingly, new advanced design methods and techniques are needed that allow engineers to leverage physics-based analysis tools to complement their experience in making conceptual decisions in an appropriate and systematic manner.

This research effort aims at developing a comprehensive multidisciplinary design optimization method to perform physics-based conceptual design of supersonic configurations. Several design methods are integrated to perform tradeoffs and analyze the results. The choice of the optimizer rested on the requirements of the supersonic aircraft design problem. As a result of an extensive literature search, the significant needs identified for potential supersonic design optimization methods are an 1) ability to handle design spaces that have multiple local optima, 2) ability to handle mixed continuous/discrete spaces, and 3) adaptability to multi-objective optimization. Genetic algorithms (GAs) are the most suitable methods to tackle all these issues simultaneously. The next section briefly presents the background for this work, and the sections after that describe the constituent elements of the design environment developed in this study. Finally, the optimization results are presented and discussed.

Received 1 July 2007; revision received 19 September 2007; accepted for publication 13 October 2007.

*Research Engineer, Aerospace Systems Design Lab. Member AIAA.
†Director and Boeing Professor of Advanced Aerospace Systems Analysis, Aerospace Systems Design Lab. Associate Fellow AIAA.

II. Background

The positive market analyses for commercial supersonic transport have reignited the passion of many companies and research units to overcome the significant technical challenges associated with the design of such an aircraft. From the high-speed civil transport (HSCT) sonic boom propagation and acceptability studies [6,7], people have realized that a small airframe such as a business jet is a stepping stone to demonstrate the technological advances necessary to meet the stringent operational requirements. The recent success of the Shaped Sonic Boom Demonstrator [8] for sonic boom reduction has provided renewed hope for a viable supersonic transport. In response to the Defense Advanced Research Projects Agency's Quiet Supersonic Platform program [9], various airframe companies have attempted to design small supersonic transports. This has resulted in a slew of patents [3–5] filed by various aircraft manufacturers. Some of these designs are given in Fig. 1. As can be seen from this figure, the proposed designs vary significantly from each other. No definite trend in the shape of the aircraft can be observed. Each design seems to have been based on experience, iteration, and redesign of a selected baseline configuration, which is different in each case. The configurations range from double-delta wing, swing wing, or continuously changing sweep-wing planforms to canard or inverted T-tail configurations. There is no unique solution to meet the design requirements. This raises the important question of how these configurations compare against each other with respect to performance and design tradeoffs. To answer this question and investigate a larger concept space, a matrix of possible alternatives for the placement and topology of components, as described in Table 1, is established. Apart from the discrete choices

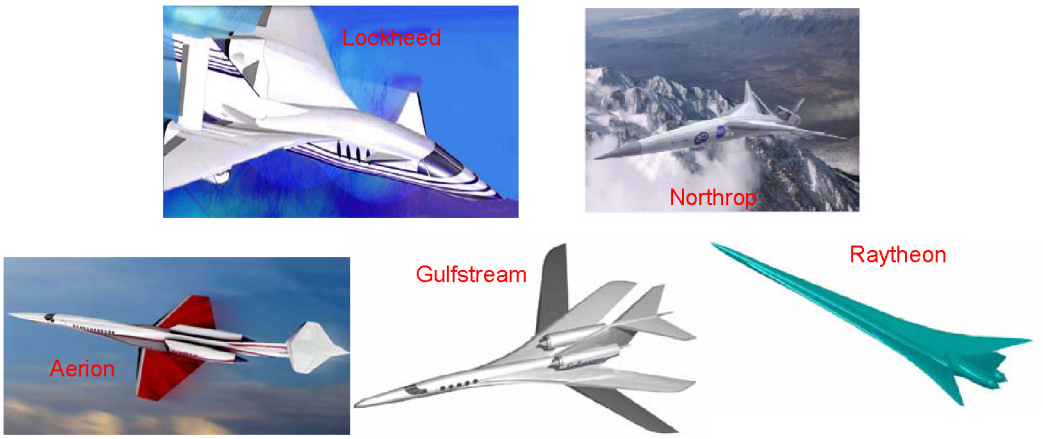

Fig. 1 Industry designs for commercial supersonic flight.

available to the designer, the design space is also defined by a large number of continuous parameters, some of which are explicitly defined in the Appendix, governing vehicle geometry and other variables. Some, such as cruise Mach number and vehicle gross weight, are common to all possible configurations, whereas other parameters, such as wing planform and kink locations, are component- and configuration-specific. Each configuration has a different number of variables defining the complete geometry.

To obtain an overall optimal design, the engine and airframe are optimized simultaneously. A GA has been developed that incorporates several operator enhancements, including two of NASA's tools: flight optimization system (FLOPS) [10] and numerical propulsion system simulation (NPSS) [11], and integrates several physics-based analysis tools to solve a multi-objective problem. The objectives considered in this study are range, sonic boom shock pressure rise, jet velocity at takeoff, approach speed, sonic boom perceived-loudness level, cruise Mach number, gross weight, stability penalty, aircraft length, and fuselage diameter. Some of these objectives are included to obtain practical configurations and others represent the performance metrics. Figure 2 shows the integration of the individual analyses into aircraft sizing and performance calculation (FLOPS). The developed environment also has the ability to allow expert input to evaluate the designs for difficult-to-quantify objectives such as aesthetics and difficult-to-compute objectives such as aeroelasticity. However, these are not discussed in the current document for the sake of brevity. After the geometry is generated using a combination of continuous and discrete parameters [12], the drag polars are generated using the aerodynamic tools and the engine deck is generated using cycle parameters and NPSS models; both of these are discussed later. These are then fed to the sizing analysis to run the aircraft configuration through the mission to obtain other objectives and responses.

III. Design Methods

During the past several years, researchers have developed various tools capable of analyzing vehicle performance. However, multidisciplinary analysis has been a problem because there is no standard format for inputs and outputs required for analysis integration. Considerable effort has been devoted in this study to assemble all the relevant disciplinary analysis tools into a single environment capable of predicting vehicle performance and environmental impact with only one input representation. This creates a geometry-centric approach to aircraft design. The following is a brief description of the different analysis modules used within the integrated simulation environment.

A. Geometry Modeling and Parameterization

Efficient geometry representation is an important consideration in aircraft design. In this study, Vehicle Sketch Pad (VSP), an enhanced version of conceptual rapid geometry modeler [13], is used. Using VSP, the designer can quickly create various aircraft geometries by assigning or changing engineering parameters, thus facilitating a more thorough search of the vehicle concept space. VSP has many features that make it ideal for use in conceptual design. These include quick creation of geometry models, a batch processing ability, the ability to create watertight geometries, the ability to perform Mach slicing, and the ability to run any geometry-based external analysis application.

B. Propulsion System Modeling

Engine-airframe integration is an extremely important aspect that is routinely ignored in conceptual studies. For every mission an aircraft might fly, there are certain configurations that would prove to better suit the different situations that the aircraft will encounter. Similar to the concept of the swing wing in the airframe, variable-cycle engines (VCE) can be developed to actually change the thermodynamic cycle, giving the effect of swapping engines in midflight. This enables each cycle to be optimized to its intended flight condition, theoretically giving a better-performing engine for the multistaged mission. Although adding this capability is beneficial, it has several penalties associated with it, such as size, weight, complexity, stability, technological risk, and overall system cost. Previous studies conducted by NASA [14] explored some of these effects to discover if the benefits outweigh the costs, and the findings led to the fixed-cycle mixed-flow turbo fan (MFTF) still being the best choice. The present study reinvestigates this topic by varying the aircraft and engine parameters simultaneously to determine which airframe/propulsion combination is optimal. There are three different engine configurations used in this study: MFTF (fixed-cycle), core-driven-fan stage (CDFS) VCE, and fan-on-blade (FLADE) VCE.

The MFTF has eight main components, as shown in Fig. 3: inlet, fan, bypass duct, high-pressure compressor (HPC), combustor, high-pressure turbine (HPT), low-pressure turbine (LPT), mixer, and a

Table 1 Matrix of configuration alternatives

Planform type	Double-delta	Ogee	Swing	Blended
Wing location	Low	Mid	High	
Pitch control	Horizontal tail	Canard	T-tail	Tailless
Engine cycle	Mixed-flow turbo fan	CDFS VCE	FLADE VCE	
Power plant installation	Under wing	Fuselage-mounted	Tail-mounted	

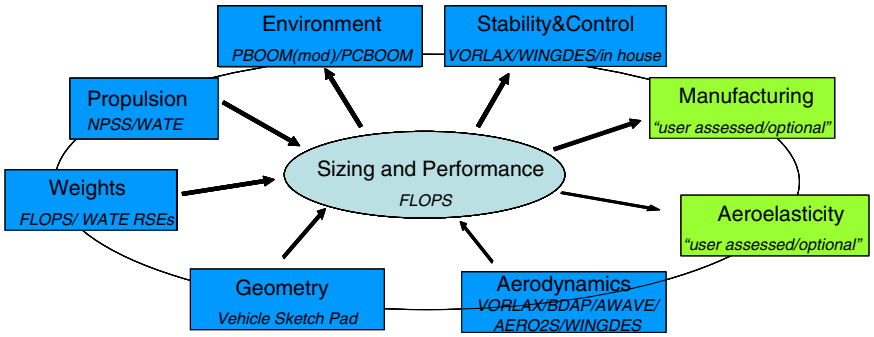

Fig. 2 Analyses setup.

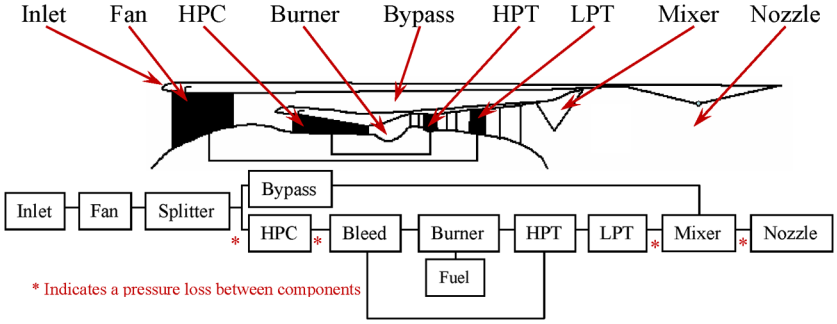

Fig. 3 Mixed-flow turbofan schematic and model.

variable nozzle. The component that defines the engine as mixed-flow is the mixer, which injects the bypass duct stream into the core flow after the turbines. Figure 3 also shows how the flow paths for this engine are modeled. The asterisk represents pressure loss between components in the propulsion model. This is one of the most common engine configurations for modern military aircraft, and it is also used in some commercial aircraft. The design bypass ratio (BPR) of the engine depends on its intended use: supersonic designs tend to have a bypass ratio of less than 1, and subsonic designs usually have bypass ratios greater than 1. The same inlet was used for all of the models. Each engine was sized for the supersonic thrust requirement and then throttled down at takeoff to meet a 7000-ft takeoff-field length requirement. As a result, mechanical suppression techniques to lower the takeoff noise signatures, such as a mixer-ejector nozzle, were not used. However, jet-velocity response is minimized by the multi-objective genetic algorithm. The strong correlation between the jet velocity and the takeoff helps the optimized configurations to proceed toward designs that meet the stringent noise goals.

The core-driven-fan stage CDFS VCE receives its name from the extra fan stage that is powered by the HPT shaft. The components that make it different from the MFTF, as well as creating its variable-cycle capability, are the CDFS, the CDFS inlet guide vane (IGV), a passive door, a bypass mixer, and a variable-area bypass injector (VABI). These can be seen in Fig. 4. The CDFS VCE engine is intended to run in either a high (or double) bypass mode or a low (or single) bypass mode. In high bypass mode, the CDFS IGV is closed, which forces the passive door to open, creating an overall higher BPR and a lower specific fuel consumption (SFC) and exhaust velocity. In low bypass mode, the CDFS IGV is open, creating a supercharged flow into the bypass duct and forcing the front door closed. This essentially creates an extra fan stage; therefore, the fan pressure ratio (FPR) is increased and the BPR is decreased. This gives the engine the capability to produce more thrust, but the SFC and nozzle velocity both increase. The complicated flow path of this engine is also illustrated in Fig. 4. The engine is intended to seamlessly switch from high bypass mode to low bypass mode in midflight when the aircraft needs more thrust as it starts its transonic and supersonic journeys. The role of the VABI is the same as the mixer in the MFTF, but in this case, a variable area is required due to the extreme changes in the bypass properties between the two modes of operation.

Fan-on-blade turbofan design has a fan that extends into an outer duct, called the FLADE duct, and sends a stream of air (only compressed by the fan) through this duct to be accelerated through a separate exhaust nozzle. A FLADE can be designed on different cores such as a turbojet, an MFTF, or even another VCE. A typical configuration of a FLADE on an MFTF core (same as in Fig. 3) is shown in Fig. 5. What gives this engine its variable-cycle

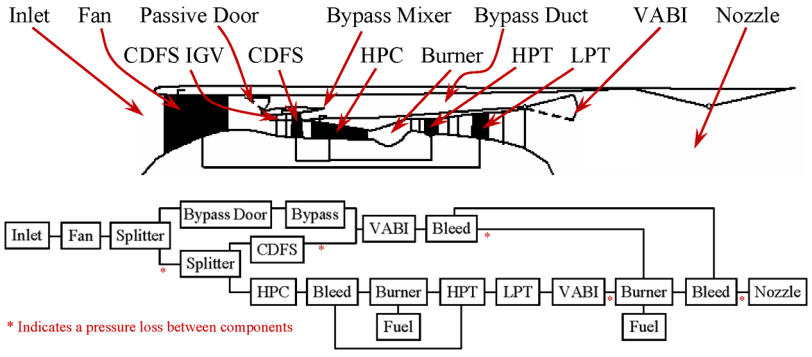

Fig. 4 Core-driven-fan stage schematic and model.

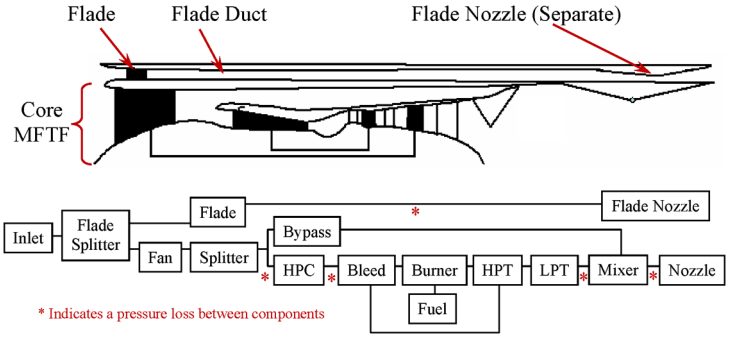

Fig. 5 FLADE engine schematic and model.

characteristics is its ability to shut off the outer bypass (FLADE) duct. This would typically be accomplished using a stator that is only in front of the FLADE duct (and separate from the fan inlet guide vane) to block air from entering the duct. Figure 5 also shows how the flow is split between the core and the FLADE duct via the splitter. Theoretically, the FLADE duct could vary from completely open to completely closed. When the FLADE duct is closed, the engine behaves similarly to the MFTF engine [15]. However, when the duct is open, the engine is in a higher bypass configuration, which is intended to produce lower SFC and lower noise characteristics. Another benefit of the FLADE design is the noise reduction attributed to the use of the FLADE duct flow at takeoff to create an acoustic shield. The ground noise signature can be lowered even more by ducting the bypass stream to the bottom of the engine, creating a thick layer of acoustic shielding [16]. The FLADE has more components than the MFTF, inherently making it more complex and heavier. Therefore, the possible performance gains have to outweigh those deficits for it to survive in the optimization environment.

For each engine architecture, the cycle design variables to be varied by the GA to determine an optimal configuration are specified in Table A1 in the Appendix. There are four design variables common to all three engines, and the FLADE and the CDFS VCE each has a variable unique to its architecture. A range for each of these variables was determined to create a realistic and comprehensive design space exploration. The fan pressure ratio range was chosen to allow for both a single-stage and a two-stage fan to be considered and to make the MFTF FPR more comparable with that of the CDFS VCE. These fan pressure ratios are reasonable for a two-stage fan. Even though transonic two-stage fans are known to have pressure ratios in the range 2.4–4.3, the upper limit of 3.26 was chosen in this study for expediency; higher pressure ratios cause a significant number of CDFS cases to fail during convergence. The overall pressure ratio (OPR) values were estimated by comparing with values of modern fighter engines. The extraction ratio (EXTR) is the ratio of the bypass stream pressure to the core stream pressure at the mixing plane. The throttle ratio (THR) is the ratio of the maximum-allowable turbine rotor inlet temperature (T41MAX) to the static sea-level design point (T41SLS). The maximum T41 was fixed to the same value for each engine. For the FLADE, the bypass ratio was chosen as the extra variable because of the effect it has on the engine performance. The range was selected based on previous NASA studies [14]. For the CDFS VCE, the extra design variable was chosen to be the CDFS pressure ratio. Its range was based on a rational limit for a single compressor stage.

The GA chooses the engine architecture and the values for the corresponding cycle design variables for each case in the population. For each case, NPSS builds the model of the engine and generates the engine deck (i.e., the table of thrust and fuel flow data required by FLOPS). The NPSS build process requires two steps: 1) a design point run at sea-level static conditions to size the engine thermodynamically and 2) an off-design run at the top of the climb to match the inlet to the engine airflow demand. It would be optimal to design each of these engines using multiple design points, preferably the supersonic cruise condition, the subsonic cruise condition, and the sea-level static takeoff condition, to create the best overall engine for the mission. This would be especially beneficial in the case of the VCEs, so that both modes of operation would have their geometry (nacelle lengths, diameter, and capture areas) optimized for their designed ambient conditions. However, due to the complexity involved, only one design point (sea-level static) was used to model the engines in this study. In the case of the MFTF, this is an appropriate way to get an engine deck; however, it should be noted that for the VCEs, NPSS has a difficult time converging when the off-design-point engine geometry varies too much from the design point. The main problem for the VCE architectures was how to get the bypass door to open at a relatively high power without causing model-convergence problems. This was accomplished by placing a lower limit on the pressure ratio, the limiting value being chosen to reduce the number of failed cases. Additional assumptions for each VCE are briefly listed in the following paragraph. MFTF engine was modeled first, due to its simplicity compared with the other cycle architectures. MFTF design served as a good basis in the design of CDFS and FLADE.

For off-design operation, the engine power management is defined for both maximum-power and part-power operation. For maximum power [also called intermediate-rated power (IRP)], the engine maintains its design-point corrected fan speed (100%) until this is overridden by the maximum T41 (T41MAX) limit. Additionally, the exhaust nozzle area is allowed to vary to maintain the design-point fan stall margin. At part power, the engine throttle (fuel flow) is allowed to vary to match a thrust target, whereas the exhaust nozzle area is held fixed at the IRP value. The thrust target is defined as a percentage of the maximum thrust [i.e., maximum thrust multiplied by percentage power represented by a power code (PC)]. Thrust is assumed to vary linearly with power code between two extremes: a maximum-power mode and an idle-flight mode. The top-of-climb point is run off-design to determine the inlet capture area match to the engine airflow demand. This ensures that the inlet spillage drag is minimized during the supersonic cruise leg. This point is run at a nominal supersonic cruise condition (cruise Mach at 55,000 ft) at 90% power. An optimizer is used to find the capture area that minimizes SFC at this condition. Thus, the effects of both inlet ram recovery and inlet spillage drag are minimized.

Once the engine model is built, the flight envelope is run to create the FLOPS engine deck. The flight envelope is an array of Mach numbers and altitudes. Mach numbers are varied from 0 to 1.8, and altitudes are varied from 0 to 65,000 ft. At each Mach number and altitude a throttle hook is run from maximum power to idle flight using the appropriate power management. All of the engine decks are created in this same fashion; however, due to the VCEs having multiple modes of operation, there were some differences in the way the power management was handled. For the FLADE at the design point, the IGV is opened, allowing NPSS to properly size the bypass duct. At off-design conditions, the maximum-power definition has two differences: first, the FLADE is intended to hold a constant corrected mass flow rate, and second, when the flight Mach number is greater than 0.92, the IGV is closed. This closes off the FLADE duct for the higher-thrust mode needed for supersonic cruise conditions. The part-power function is identical to that of the MFTF, except that again the FLADE duct is closed when the flight Mach number is greater than 0.92. The CDFS power management was handled

differently from the FLADE. Instead of changing the mode of operation at a specific Mach number, it is controlled by the power setting. At full power, the blocker door is set to closed, and the CDFS IGV is kept open. Once the power setting drops below about 90%, chosen according to a cutoff pressure ratio that allows solver convergence, the blocker door is then open and the CDFS IGV is closed, creating the high bypass mode.

C. Other Analyses

1. Aerodynamics

A number of conceptual aerodynamic tools based upon linearized methods are used to calculate properties such as supersonic wave drag (AWAVE) [17], induced drag (WINGDES) [18], skin-friction drag (BDAP) [19], and low-speed aerodynamics (AERO2S) [18]. Several secondary sources of drag, such as form drag and transonic wave drag, are not accounted for by these programs, and they are calculated using handbook methods from Raymer [20]. Once the geometry is generated and the aerodynamic quantities are calculated using the preceding methods, the relevant data are written into a FLOPS file. The geometry includes not only airframe but also propulsion data, such as the longitudinal and lateral locations of the engines, nacelle diameter, and the overall nacelle length. The locations are obtained by the optimizer from the limits imposed on the relevant design variables. The diameter and length are obtained from the engine-weight regressions discussed in a subsequent section. The geometry data are then used during the sizing and mission analyses phase of the design, instead of the aerodynamics module included within FLOPS.

2. Sonic Boom

Design of a commercial supersonic aircraft invariably involves sonic boom analyses. In this study, PBOOM [21] and PCBOOM [22] are used. To simulate the atmospheric absorption, a rise time of 3 ms is assumed for a shock strength magnitude of 1 psf. This is based on an empirical model fit based on experimental data [23] to account for atmospheric attenuation and molecular relaxation.

3. Stability and Control

Stability is an important consideration in aircraft design, even today, after the advent of fly-by-wire systems, because there can often be severe performance penalties if the vehicle is not properly balanced. In conceptual design, the exact location of each subsystem within the vehicle is not calculated, and so historical data are used to place them for the purposes of center-of-gravity (c.g.) calculations. It is known that for static stability, the center of gravity must be ahead of the neutral point of the aircraft. In this study, neutral points (center of lift) are calculated using AERO2S and WINGDES. The stability penalty is calculated to be the area enclosed by the center-of-lift lines and the c.g. envelope The optimizer attempts to minimize this response.

4. Weights

Weight analysis is still a difficult task for conceptual designers. Though several codes such as equivalent laminated-plate solution (ELAPS) [24] have been developed for predicting structural weight, studies have not conclusively shown that the results of these codes are more accurate than the much simpler methods based upon historical data and simple beam theory such as those used in FLOPS. This fact led to the use of the FLOPS weight module for empty-weight prediction, though it is recognized that a more detailed structural and weight analysis will need to be performed on the resulting concepts before proceeding to preliminary design.

Apart from computing the weights associated with the airframe, the propulsion system weights are also required. This was done by modeling an MFTF using weight analysis of turbine engines (WATE) [25]. The code was originally developed by the Boeing Military Aircraft Company in 1979. Improvements to the code were later added by NASA and McDonnell Douglas Corporation [26]. The code uses semi-empirical methods augmented by analytical calculations for specific component elements.

To reduce environment run time and complexity, surrogate models of WATE are generated. To create the regressions, the MFTF engine-cycle design variables FPR, OPR, THR, and EXTR were varied and engine weight normalized by baseline thrust was recorded. Specifically, a four-level full factorial design of experiments was run with the ranges shown in Table A1. These regressions provide engine weight over baseline thrust, nacelle diameter over baseline thrust, and nacelle length. The first two are functions of FPR, OPR, EXTR, and THR, and the nacelle length has an additional variable in cruise Mach number. The engine weight obtained from the regressions includes the nozzle and accessories weight, but not the inlet weight. To account for the inlet weight, an additional 2024.0 lb is added to the weight obtained from the regressions. Weight normalized by thrust was used so that the regressions would not be entirely dependent on the mass flow rate chosen in the NPSS engine model. For moderate variation in mass flow rate and nominal values of the engine-cycle variables, the normalized weight remains relatively constant over a range of mass flow from 700 to 1000 lb/s. In this study, all engine models in NPSS were modeled with a mass flow rate of 1000 lb/s. The thrust and weight values were then scaled down later in the environment by FLOPS to reflect more realistic values of mass flow rate. Scaling thrust can lead to incorrect SFC and weight estimates. SFC may be incorrect because, beyond a certain point, losses do not scale. A similar argument may be applicable to the weight of structural components. However, for this study, these effects are believed to be small, because the original loss and weight estimates were made for airflows sized nearer to the true values of the baseline case.

A surrogate model using first order, second order, and first-order interaction effects is obtained by eliminating the parameters that do not affect the response. These can be identified by examining the p-value of each parameter, listed under the parameter estimates in Fig. 6a. Using a cutoff α level of 0.10, parameters with a p-value greater than 0.1 were eliminated from the model. Using this criterion, the number of parameters in the model was reduced from 19 to 9, excluding the intercept term. The R^2 value remains the same (0.983) as obtained using all the parameters, but now the model is simpler. The parameters in Fig. 6a and their corresponding coefficients make up the final regression used to predict the engine weight of the MFTF. The graph shows the actual value versus the model-predicted value. Four clumps of points can be seen in the figure. This is explained by the nature of the simulation experiments. Recall that the experiment was a four-level full factorial, with each variable taking on four different evenly spaced values. If more random points were run, then less clumping would be observed. Regardless, the points lie mostly along the diagonal, indicating that actual values in the design space closely follow their corresponding predicted values. Additionally, the distribution of residual of the model is examined in two different plots. The model fit error is calculated for all the 256 points used to create the model. Ideally, the error of a model should be normally distributed with a mean around zero. Figure 6b shows the details of the model-fit-error distribution. The mean 0.082% is very close to zero. The standard deviation is 3.85%, and no point is off by more than 8.68%. The model fit error alone does not explain the predictive power of the model. To evaluate the predictive power of the model, the model representation error is considered. A model representation error is calculated for new data points that were not used in fitting the data; 80 new points were run through WATE and their responses recorded. The details of the model representation error are shown in Fig. 6c. The distribution is not normal, but still resembles a normal distribution, excluding the center. Interestingly, the standard deviation actually improves to 3.385%. The mean moves slightly further away from 0 to 0.55%, but this is still certainly acceptable. Also, the worst error is only 5.83%. From these data, it was concluded that the model has sufficient accuracy and predictive power.

After the MFTF engine weight is predicted, FLADE and CDFS VCE engine weights are predicted by multiplying the MFTF engine weight by a scaling factor. The scaling factor for the FLADE engine

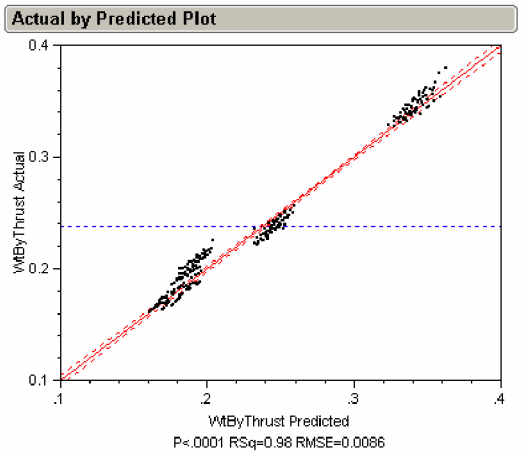

Summary of Fit

RSquare	0.983488
RSquare Adj	0.982884
Root Mean Square Error	0.008642
Mean of Response	0.238486
Observations (or Sum Wgts)	256

Analysis of Variance

Source	DF	Sum of Squares	Mean Square	F Ratio
Model	9	1.0941814	0.121576	1627.999
Error	246	0.0183708	0.000075	Prob > F
C. Total	255	1.1125522		<.0001*

Parameter Estimates

Term	Estimate	Std Error	t Ratio	Prob>|t|
Intercept	0.3526925	0.021633	16.30	<.0001*
FPR	-0.113248	0.000993	-114.1	<.0001*
(FPR-2.53)*(FPR-2.53)	0.0861182	0.00228	37.76	<.0001*
OPR	0.0015765	0.000145	10.88	<.0001*
(FPR-2.53)*(THR-1.05)	0.1882343	0.026635	7.07	<.0001*
EXTR	0.0717849	0.014492	4.95	<.0001*
(FPR-2.53)*(EXTR-1)	-0.068167	0.026635	-2.56	0.0111*
THR	0.0275876	0.014492	1.90	0.0581
(THR-1.05)*(FPR-2.53)*(OPR-30)	0.0133011	0.007147	1.86	0.0639
(THR-1.05)*(THR-1.05)	-0.887741	0.486117	-1.83	0.0690

a) Model fit summary after removing inconsequential variables

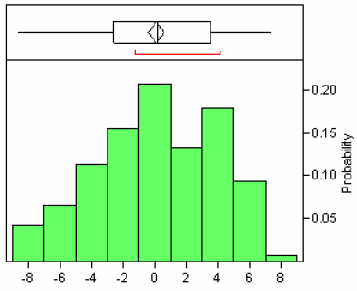

Quantiles

100.0%	maximum	7.409
99.5%		7.333
97.5%		6.380
90.0%		5.042
75.0%	quartile	3.526
50.0%	median	0.186
25.0%	quartile	-2.642
10.0%		-5.232
2.5%		-7.559
0.5%		-8.655
0.0%	minimum	-8.680

Moments

Mean	0.0817946
Std Dev	3.8450412
Std Err Mean	0.2403151
upper 95% Mean	0.5550496
lower 95% Mean	-0.39146
N	256

b) Model fit error

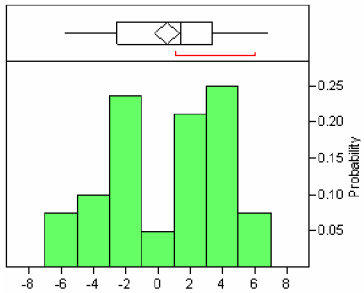

Quantiles

100.0%	maximum	6.866
99.5%		6.866
97.5%		6.479
90.0%		4.771
75.0%	quartile	3.412
50.0%	median	1.381
25.0%	quartile	-2.550
10.0%		-3.426
2.5%		-5.734
0.5%		-5.828
0.0%	minimum	-5.828

Moments

Mean	0.5522769
Std Dev	3.3852097
Std Err Mean	0.376478
upper 95% Mean	1.3056185
lower 95% Mean	-0.201065
N	80

c) Model representation error

Fig. 6 Engine-weight-regression model.

weight used in this study is 1.2. For the one-stage-fan CDFS VCE (i.e., with FPR <1.8), the scaling factor is assumed to be 1.042, and for the two-stage-fan CDFS VCE (i.e., with FPR ≥ 1.8), the scaling factor is chosen as 1.3. These scaling factors had to be incorporated because WATE cannot model the VCE components. For example, the bypass door must be modeled as a simple duct so that the weight of the moving parts is not captured. The same is the case with the variable-area bypass injector (VABI). The CDFS-stage weight is not computed properly, because associated frames, disks, bearings, etc., are not accounted for correctly. These factors have been treated manually for a baseline engine, and the differences were combined into a scale factor to be applied to an MFTF model that otherwise has the same cycle parameters of the VCE models. The authors realize that these scale factors are somewhat subjective. But due to the lack of a proper tool to model complex VCE propulsion system weights, calibrated scale factors for baseline design were used in this study.

5. *Mission Analysis*

FLOPS is used to perform mission analysis. The mission investigated in this study is a split subsonic/supersonic mission with a desired total range of 4000 n mile. The first 1500-n-mile segment of the mission is the subsonic leg (including climb), with a cruise speed of Mach 0.92. The remainder of the mission includes the supersonic climb, a supersonic cruise at a Mach number in the range of 1.6–1.8, and descent. This approximates the realistic missions for which a supersonic business jet would be desirable for accelerated travel. Because of the Federal Aviation Administration (FAA) regulations on noise and supersonic travel over land, an aggressive supersonic mission was not chosen; this will be studied in subsequent efforts. With the desired total range for the mission being 4000 n mile, approximately 2500 n mile is needed for the supersonic cruise (including the descent). In this study, the takeoff gross weight (TOGW) is set by the GA for every run; therefore, the aircraft flies a 1500-n-mile subsonic leg and then flies as far as it can in the supersonic leg, sometimes exceeding the desired 4000-n-mile threshold and sometimes falling short. Scaling of the engine, on the other hand, is performed through the use of the engine deck created by NPSS and the scaling laws imbedded in FLOPS, which scale the engine data to the thrust level that is necessary to execute the mission performance module and takeoff and landing module.

D. Advanced Genetic Algorithms

In engineering design, there are almost always multiple criteria that must be considered during the concept selection process. Objectives such as weight, cost, and speed must be balanced against each other to find the appropriate combination that will result in a successful design. Traditionally, these problems are handled by creating an aggregate objective function, the so-called overall evaluation criterion. However, this method cannot numerically quantify how important the objectives are in relation to each other, resulting in designs that do not really best meet the designers goals. Multi-objective genetic algorithms attempt to solve this problem by using the concept of Pareto-optimality to find nondominated solutions. A solution is said to be nondominated when there is no other solution in the space that is better with regard to all decision variables. The set of nondominated solutions, or Pareto front, makes up a hypersurface along which improvement in one objective requires a sacrifice in another. Once this front has been found, the engineer can use it to explore the relationship between the objectives so that intelligent decisions can be made.

Several modifications to the conventional GA, such as the strength Pareto evolutionary algorithm (SPEA) [27], have gained widespread acceptance for use in the multi-objective optimization problem. This algorithm incorporates elitist and population-diversifying characteristics to multi-objective Pareto optimization. The SPEA2 algorithm balances the diversification of the population as well as exploits solutions from an archive of elite designs. However, as the number of objectives increases, the proportion of nondominated designs also increases. Recent research [28] has shown that although GA operators work well for two or three objective problems, their effectiveness drops significantly when there are a large number of conflicting objectives. The SPEA2 algorithm becomes ineffective under these conditions. This is because the proportion of the population that is nondominated grows exponentially as the number of simultaneous objectives increase. In fact, Deb [29] found that as the number of objectives grows, nearly all solutions become nondominated and would therefore have equal fitness values. Because of reliance on dominance-based fitness, most multi-objective algorithms have difficulties solving problems with more than two or three responses.

According to the definition of nondominance, a solution is nondominated if no other solution in the set is better in any objective without being inferior in at least one other objective. This definition of dominance does not deal with magnitudes. A solution that trades a large amount of capability in one objective for an infinitesimal amount of gain in another is not penalized by the fitness-assignment schemes used by many of the common evolutionary algorithms in literature.

1. Multi-Objective Optimization

In response to the poor performance of the multi-objective evolutionary algorithms available in literature, an advanced genetic algorithm method has been developed. Rather than optimizing each of the M objectives, the problem is reformulated to solve for the tradeoff between M biased aggregate functions that favor attainment of one particular objective but do not ignore performance of the other M-1 objectives. Goal programming [30] is used in the current study as the aggregation technique. In this method, three parameters per objective are specified: a goal or ideal value, a normalization value obtained using sampling, and a weighting value to specify importance. The goal value corresponds to the minimum level of performance in a given metric that would be considered acceptable. The problem is then recast as the minimization of the weighted difference between the actual and goal values, as shown in Eq. (1). Goal programming may be understood to be analogous to a weighted target-matching problem:

$$V_i(x) = \left(\sum_{m=1}^{M} w_m \left| \frac{f_m(x) - g_m}{n_m} \right|^p \right)^{1/p} \tag{1}$$

where w_m is a vector of weights, g_m is a vector of goal values, and n_m is a vector of normalization constants. In the present study, all the objectives were equally weighted. The conceptual design process for the desired supersonic transport does not have a standard set of requirements or goals, unlike many traditional subsonic design efforts. Certain well-accepted guidelines, as shown in Table 2, are used in this study as design goals. The normalization constants were determined by calculating the variance of each objective for a random population of individuals and then rounding that value to a convenient number. The normalization values allow for the width of the distribution to be taken into account, thus including a convenient way to scale the objectives in an unbiased manner.

Table 2 Objective goals and weights

Objectives	Goal value	Normalization value
Range, n mile	4200	1.0
Gross weight, lb × 1000	100	50.0
Jet velocity for 7000-ft takeoff, ft/s	900	2.0
Cruise Mach number	1.7	0.0025
Shock pressure rise, psf	0.35	0.002
Sonic boom, PL (dB)	88	0.01
Approach velocity, kt	140	0.1
Length, ft	140	0.1
Static stability penalty	100.0	10.0
Cabin diameter, ft	6.9	0.001

2. Operator Enhancements

As has been mentioned earlier in this paper, one of the objectives of this work is to study the tradeoffs associated with component placement. The GA not only attempts to optimize the component shapes, but also their placement, implying that the optimization problem is a mixed discrete/continuous hierarchical problem. It is found through experience that the conventional GA crossover operators yield very poor performance for such a problem, due to excessive chromosome disruption. To overcome this, several operator enhancements have been included in the GA. Conventional GAs use binary encoding to discretize the computational domain before searching for optimum locations. However, application of binary encoding to variables with discrete settings requires specification of several special cases, which can cause the procedure to become inefficient. To overcome this problem, real-valued genetic algorithms are used in this study.

Although evolutionary algorithms have been applied to several engineering design problems, not many studies have looked at optimizing problems that have both the system architecture (discrete) and design (continuous) variables. One specific instance of combining discrete and continuous variables in evolutionary optimizers is described by Parmee [31], termed structured genetic algorithms. Unfortunately, the structured GA quickly focused on a single alternative, even for relatively small design hierarchies. The tendency to quickly focus on a small portion of the design space may result in the algorithm overlooking potentially promising solutions. This deficiency was addressed with a method called the hybrid structured genetic algorithm [31], which introduced variable mutation probabilities to the discrete and continuous variables. This method used a bitwise mutation probability of 20% for discrete variables and a much lower mutation probability of 2% for continuous variables. The large mutation probability applied to the discrete variables effectively maintained genetic diversity, but may also prevent efficient convergence because of the mutation operator's tendency to move away from good solutions.

The crossover operator is applied to a postreproduction population to cross genes between its members. The aim of this operator is to attempt to create better designs by swapping genes (design variables); the idea is to insert a good gene from one design into another design and increase its fitness value. Several choices exist for real-variable crossover, such as uniform linear, bilinear (BLX-α) [32], simulated binary (SBX) [33,34], or an enhanced version of simulated binary (vSBX) [35]. Going into the details of each of the

crossover schemes is beyond the scope of the present study; complete details are presented in the cited references. In this study, the enhanced version of the simulated binary crossover scheme (vSBX) is used. The justification for this is provided in Fig. 7. Four different crossover schemes are compared by starting with two parents, (5.0, 5.0) and (10.0, 10.0), and allowing repeated crossover operations. The resulting offspring are depicted as small dots. It is seen that uniform linear operator explores the domain without preference given to the location of parents and the BLX-α operator does the same, except it explores a slightly larger domain. The SBX operator produces offspring that are concentrated more around the parents; however, it fails to explore the design space thoroughly, leaving out the top left and bottom right quadrants of the design space. The vSBX operator has the desired characteristics of both design space exploration and clustering near the parent designs.

Simple crossover types do not guarantee a good design space exploration for hierarchical problems. This prompted the development of a new type of hierarchical crossover [36] in which the vSBX crossover is implemented over components of the same category type (for example, if both aircraft have variable geometry wings), but the components are swapped with 50% probability if dissimilar (one parent has a canard and one has a T-tail). Figure 8 depicts an example in which two parents of dissimilar topologies undergo hierarchical crossover to produce two offspring. Results have shown that this method allowed useful genetic information transfer with minimal gene disruption.

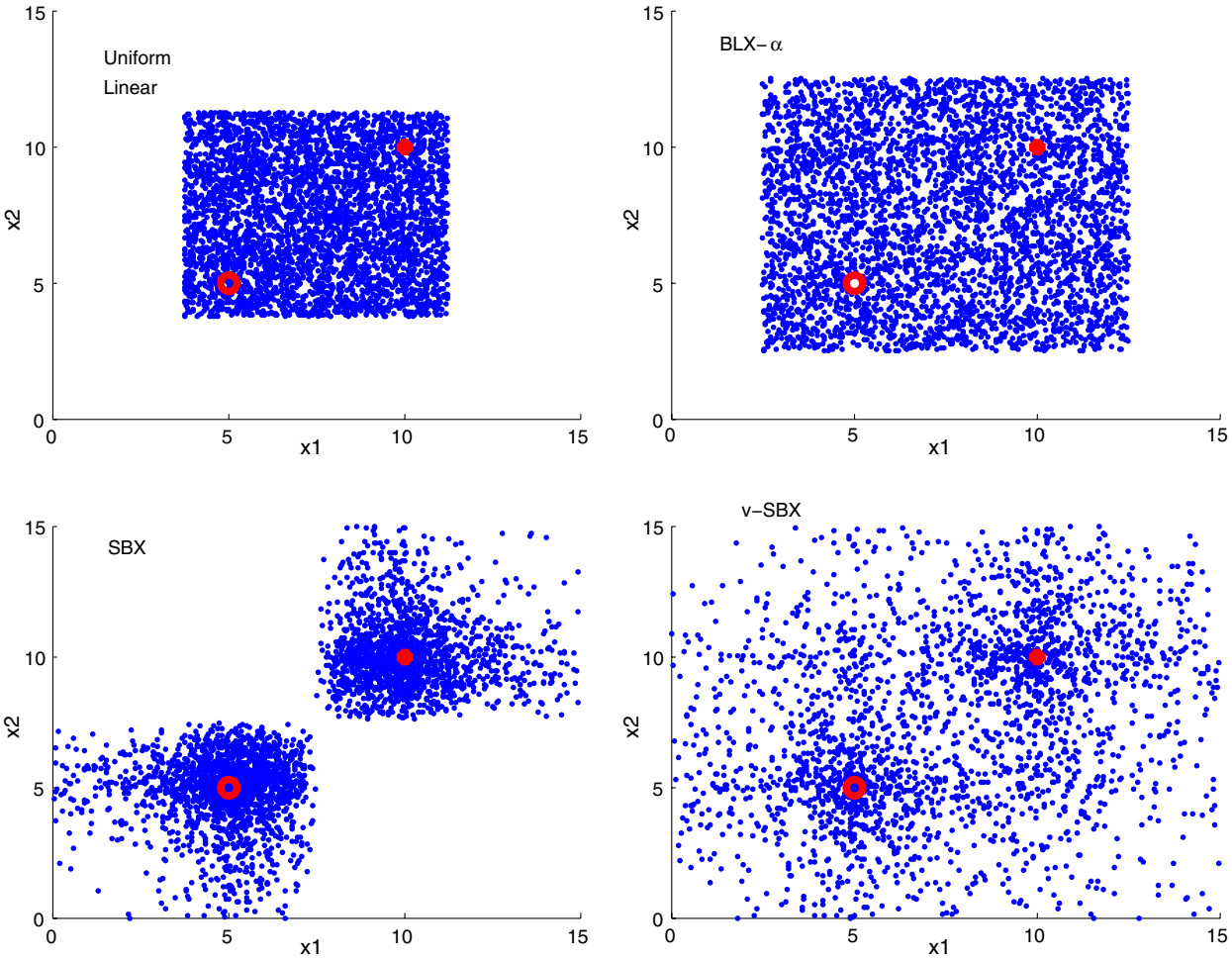

Fig. 7 Comparison of design exploration ability of crossover schemes.

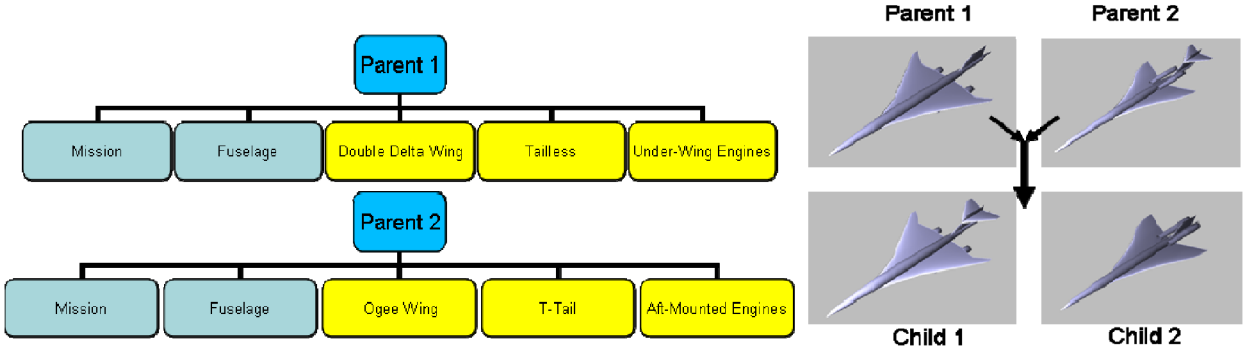

Fig. 8 Hierarchical crossover scheme [36].

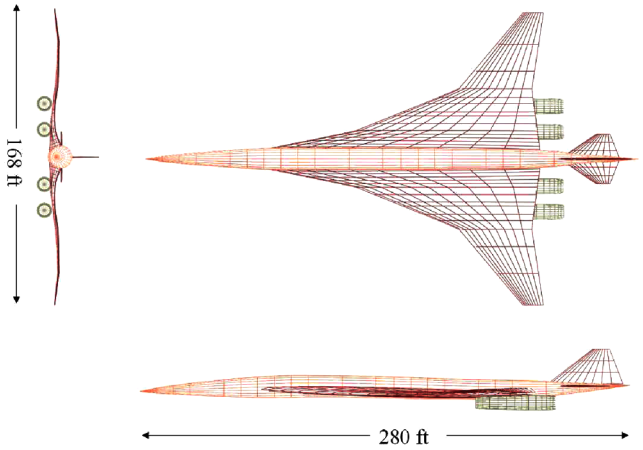

Fig. 9 Three views of the supersonic reference vehicle provided by NASA [36]

Maintaining population diversity is another important issue in using GAs. Restricted tournament replacement [37] is used in this study to allow a diverse population. Under this method, each child solution is compared with ω solutions from the parent population and replaces the closest of these if it has better fitness. Conventional tournament selection picks parent designs randomly and causes crossover between these possibly dissimilar parents, which might disrupt the evolutionary improvement desired in the subsequent populations. To avoid this, mating restriction is applied using a mating-selection algorithm that biases the selection phase of the algorithm to prefer and cross more phenotypically similar parents [38]; α solutions are chosen via standard binary tournament selection with replacement. Of these α candidates, the solution that is most similar or dissimilar from the others is chosen as the first parent. The mate for this first parent is biased by performing β fitness-based tournament selections and then selecting the winner closest to the original parent, as measured in genotypic space. By increasing the magnitude of β, the user increases the strength of similarity between parent solutions. Positive values of β are of special interest for problems with hierarchical encodings, because crossover between similar solutions is expected to produce children with better fitness values.

Table 3 Technology weighting factors used in weight modification

Multiplication factor	Value
Wing weight	0.75
Fuselage weight	1.05
Empennage weight	0.85

Table 4 Weight analysis comparison [36]

Mass and balance summary	Calculated	Reference	% difference
Wing	74,621	84,278	−11.46%
Horizontal tail	2952	3084	−4.28%
Vertical tail	2375	2385	−0.42%
Fuselage	49,996	49,996	0.00%
Landing gear	29,998	27,908	7.49%
Nacelle (air induction)	0	0	
Structural total	159,942	167,652	−4.60%
Engines	87,339	89,438	−2.35%
Thrust Reversers	0	0	
Miscellaneous systems	1463	1463	0.00%
Fuel system: tanks and plumbing	5443	5026	8.30%
Propulsion total	94,245	95,926	−1.75%
Surface controls	9132	9130	0.02%
Auxiliary power	1192	1192	0.00%
Instruments	1366	1546	−11.64%
Hydraulics	5143	4301	19.58%
Electrical	4399	4542	−3.15%
Avionics	1983	2718	−27.04%
Furnishings and equipment	18,987	19,825	−4.23%
Air conditioning	5449	5504	−1.00%
Anti-icing	483	363	33.06%
Systems and equipment total	48,134	49,121	−2.01%
Weight empty	301,779	312,700	−3.49%
Crew and baggage: flight, 2	450	675	−33.33%
Crew and baggage: cabin, 4	665	975	−31.79%
Unusable fuel	1574	1896	−16.98%
Engine oil	367	367	0.00%
Passenger service	2681	3318	−19.20%
Cargo containers	1575	1575	0.00%
Operating weight	309,091	321,506	−3.86%
Passengers, 175	28,875	28,875	0.00%
Passenger baggage	7700	7875	−2.22%
Zero fuel weight	345,666	358,256	−3.51%
Mission fuel	468,232	455,642	2.76%
Ramp (gross) weight	813,898	813,898	

3. *Multi-Island Strategy and Parallelization*

Two of the most frequent criticisms of genetic algorithms are that they typically require a very large number of function evaluations to converge and they are prone to premature convergence in certain circumstances. In an attempt to accelerate the convergence of genetic algorithms, an injection island strategy has been proposed, which

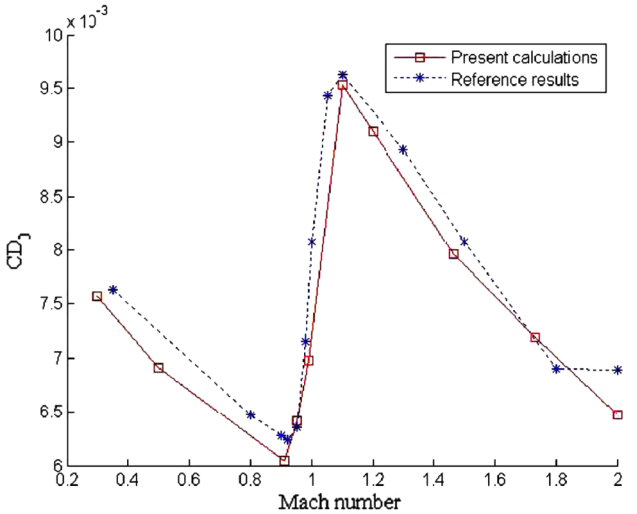

a) Zero lift drag comparison at 50,000 ft

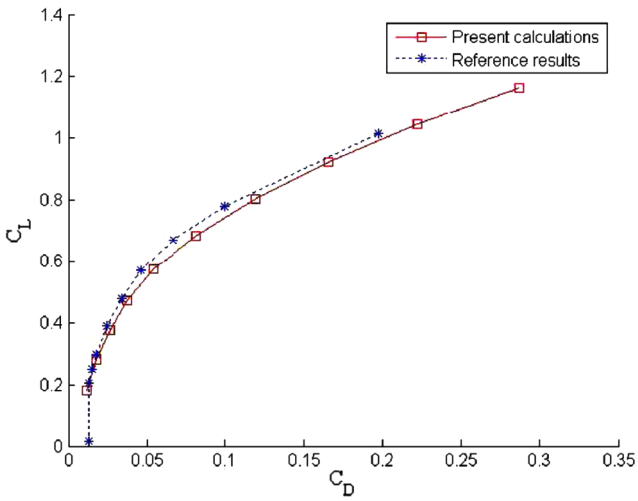

b) Takeoff drag polar comparison

Fig. 10 Aerodynamic validation with the reference vehicle [36].

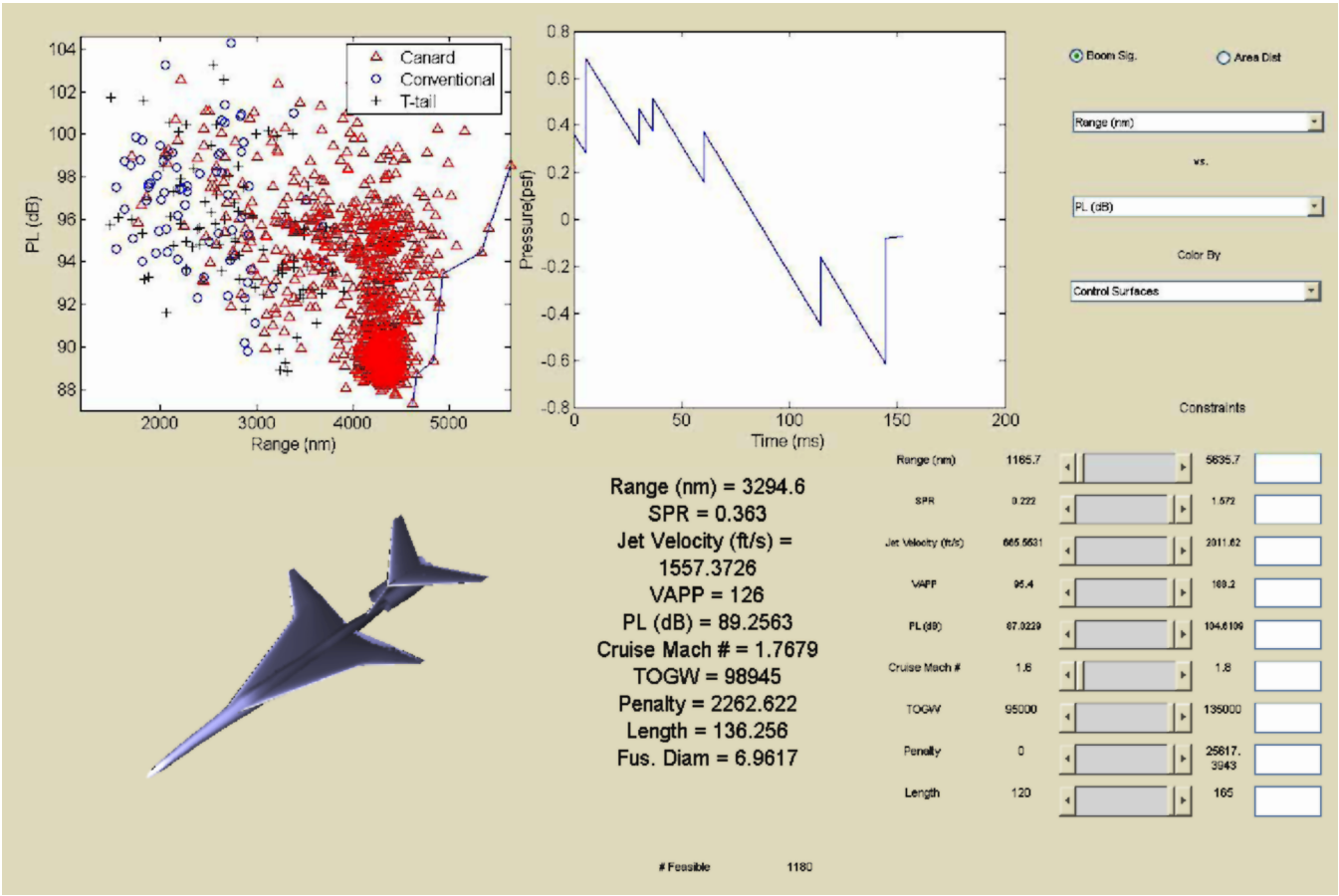

Fig. 11 Canard performance comparison, visualization, and tradeoff.

allows multiple populations to evolve in parallel [39]. In this scheme, the main GA population evolves normally using the GA operators and secondary populations are run at regular intervals, and the best results from those are injected into the main GA population. This optimization scheme has been shown to improve the convergence rate by nearly an order of magnitude when compared with the conventional GA. This scheme is used in this study to improve the performance of the GA. Because of the size of the problem, the entire process could take a long time to run on a single computer. To remedy this issue, parallel-grid computing using CONDOR [40,41] has been used in this study.

E. Optimization Setup

The optimization process begins by creating multiple populations. In this study, the main population is augmented by a single secondary population. Each population member represents a complete geometry, along with propulsion parameters and certain flight conditions. The engine model is run and the engine deck is generated. Engine-weight regressions are used to calculate the propulsion system weights. The aerodynamics, stability, noise, and other relevant analyses are run over each geometry. FLOPS runs the geometry through a representative mission by parametrically varying the thrust-to-weight ratio (TWR) to minimize the excess fuel. The calculated thrust-to-weight ratios are use to scale the engine deck. FLOPS is run using the scaled engine deck and drag polar information. The altitude is allowed to vary to maximize range. Finally, the engine takeoff power setting is estimated by iterating FLOPS to take off around 7000 feet. This was done to compare different engine-cycle architecture for takeoff noise. Although noise was not considered explicitly during this study, inclusion of jet velocity as one of the objectives makes the final designs acceptable in that dimension because of the strong correlation between takeoff noise and jet velocity.

Table 5 Effect of horizontal stabilizer type

Objective	T-tail	Canard
Range, n mile	3330.7	4362.6
Jet velocity for 7000-ft takeoff, ft/s	1554.45	1420.8
Shock pressure rise, psf	0.32	0.33
Sonic boom, PL (dB)	88.447	94.848
Approach velocity, kt	137.9	133.1
Static stability penalty	2577.75	168.2

IV. Validation

To ensure that the tools and methods being used for the work are consistent with those used by other researchers for supersonic aircraft analysis, a supersonic reference geometry provided by engineers at NASA was analyzed using the modeling environment. The reference vehicle, shown in Fig. 9, is based upon a concept developed during the High-Speed Research Program. It has been resized to carry 150 passengers over a 5500-n-mile, 50% Mach 0.95, 50% Mach 2.0 mission. The power plant was also supplied by NASA and includes a mixer-ejector nozzle sized to meet FAA stage-III noise levels. To simulate present-day composite technology effects, the technology weighting factors listed in Table 3 were applied to the weights computed by FLOPS. These same factors were used to generate the NASA-supplied results. To obtain results for comparison, the present modeling environment was run in analysis mode with the same gross weight as that of the supplied reference vehicle.

A. Weight Comparison

Table 4 depicts the comparison between the weight breakdown from the NASA reference with those calculated using the analysis tools mentioned earlier in this paper. The predicted weights are

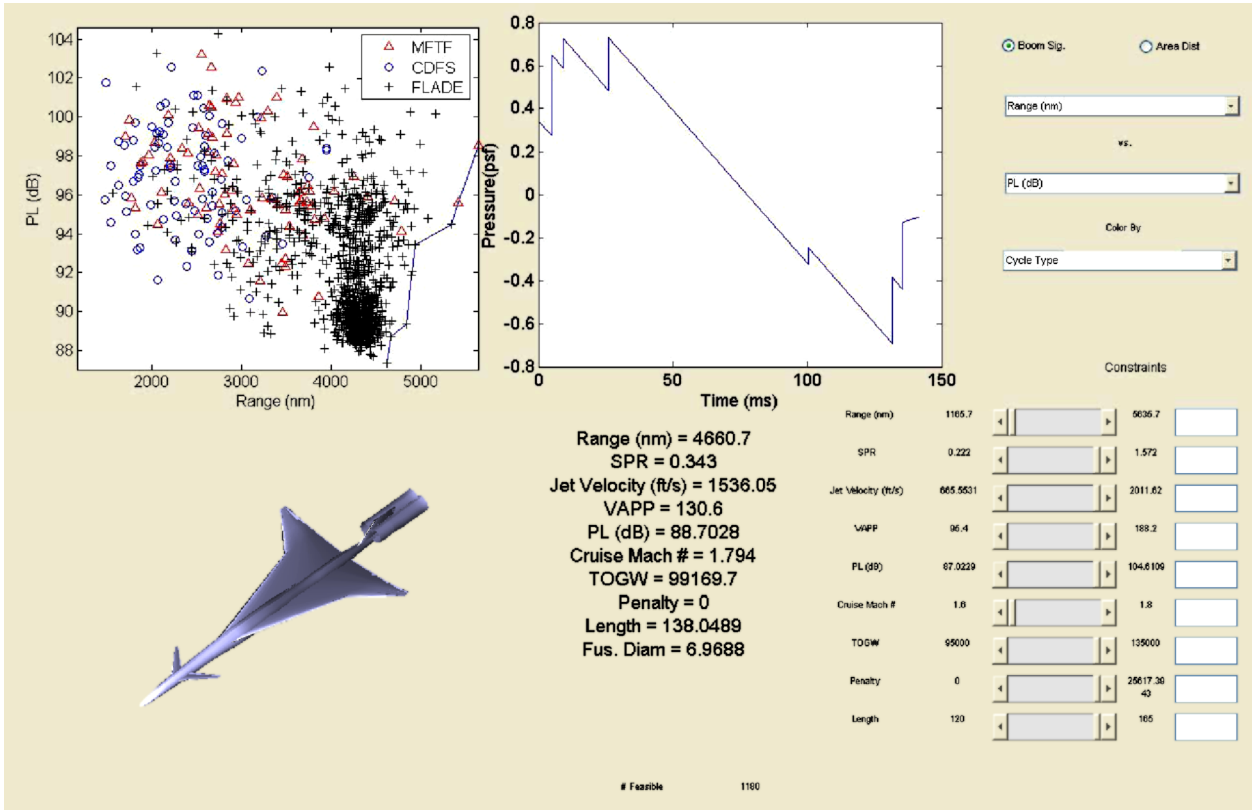

Fig. 12 Cycle comparison and visualization.

similar, with an empty-weight difference of about 3% between the two models. Individual subsystems exhibit more variability and therefore warrant additional analysis. The wing weight and landing gear weight vary significantly from the reference values. The difference in predicted wing weight between the two models accounts for the majority of the total empty-weight discrepancy. This discrepancy is attributed to the choice of wing sweep location as the independent variable; our study uses the trailing-edge sweep as suggested in [42], whereas the NASA reference used the 3/4-chord sweep to determine the wing weight. The independent parameter was changed to 3/4-chord sweep and it was determined that the wing weight matched closely with the reference; however, the trailing-edge-sweep location was retained to be used in the actual calculations. The difference in landing gear weight was investigated and found to arise from the fact that the current model is designed using a slightly higher maximum landing weight. There are several other entities, such as avionics, that vary significantly between the models in a percentage of bases, but their absolute difference is small and therefore not deemed important for further study. Overall, it appears that the current results largely agree with those that were previously generated by NASA.

B. Aerodynamics Comparison

As seen in Figs. 10a and 10b, the aerodynamic data generated using the tools described earlier in this paper matched fairly closely with those generated by NASA. In some cases, there were some minor differences, such as in subsonic zero lift drag. This is mainly due to the fact that the drag polars used in the reference configuration were scaled within FLOPS, whereas those used in the present analysis were not. Other minor differences may also be due to the use of different empirical corrections, such as that used to account for subsonic form-factor drag.

Table 6 Propulsion system parameters for comparison

Variable	FLADE	CDFS	MFTF
FPR	2.598	1.6242	2.598
OPR	29.834	29.834	29.834
TTR	1.0552	1.0552	1.0552
EXTR	1.0217	1.0217	1.0217
FLADE bypass	0.2		
CDFS PR		1.6	

V. Results

The results generated from the GA can be used to study various tradeoffs and other geometry-topology-dependent effects. Once the GA is terminated, the representative concepts from the Pareto-optimal front can be analyzed thoroughly to make suitable conceptual decisions. The requirements and topology impacts on the concept selection process can be studied in detail. Specifically, the impact of control surface configuration, engine-cycle type, and wing planform are some of the important effects that are subsequently discussed. The primary population of the GA has a population of 300 and is run for 40 generations. After every five generations, a secondary population of 200 was run for 30 generations, and the best results from the secondary optimization are combined with the primary population to pick the best 300 from the combined group. As

Table 7 Effect of propulsion cycle on system responses

Variable	FLADE	CDFS	MFTF
Range, n mile	4154.2	2602.8	3385.6
Jet velocity for 7000-ft takeoff, ft/s	1405.1	1252.2	1181.5
Shock pressure rise, psf	0.31	0.457	0.619
Sonic Boom, PL (dB)	87.597	92.586	93.256
Approach velocity, kt	132.8	133	132.3
Static stability penalty	26.64	1393	1240.8
Empty weight, lb	43,481.1	50,431.9	46,618
Thrust per engine	19,048.8	22,576.5	27,868.2
Engine scale factor	0.438	0.48	0.6123
TWR	0.386	0.457	0.564

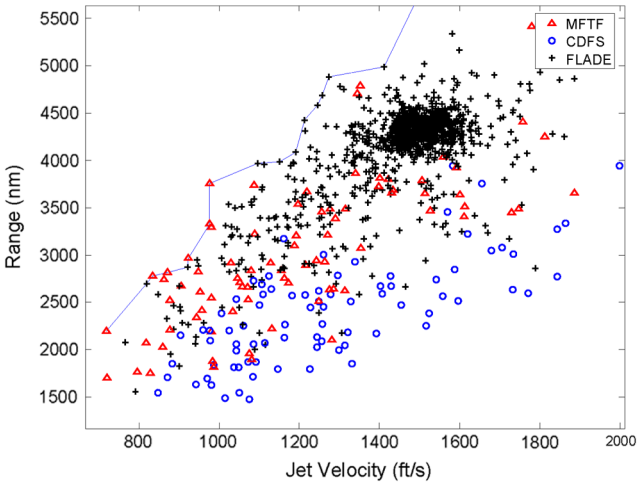

a) Jet-velocity and range tradeoff

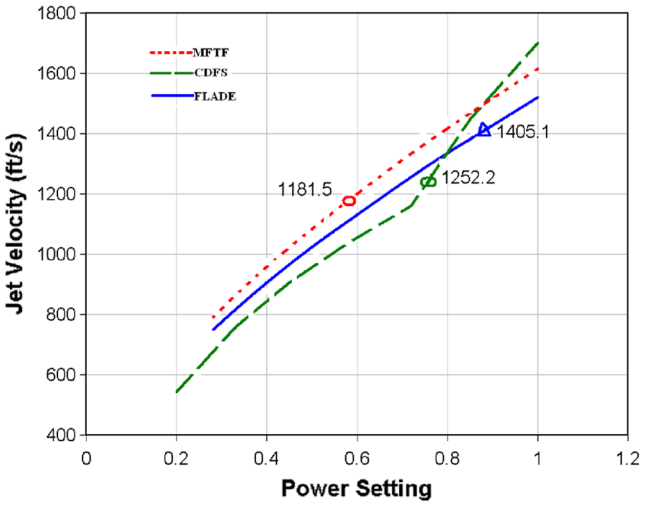

b) Exit velocity comparison

Fig. 13 Comparison of engine cycles in the range/jet-velocity dimensions.

mentioned earlier, the grid computing architecture of CONDOR was used. The grid consisted of 50 computers with Intel Pentium IV compilers, each with a RAM of 512 MB. The total number of function evaluations performed for the algorithm were 12,000 for the primary population and 48,000 for the secondary populations. Each function evaluation takes approximately 90 s on a single computer. Therefore, if a single computer were used, it would take 62.5 days. Using the grid architecture, all the runs were accomplished in 2.05 days, thus producing a speedup of 30.48. The average sublinear speedup can be attributed to a certain extent to the working setup of CONDOR and its job allocation. Other parallel architectures may be used to achieve much higher speedups and therefore possible overnight runs. This was not done at the time this work was completed.

A. Canard Tradeoffs

The effect of a canard is studied using Fig. 11. It is seen that the GA picks canard configurations; a few T-tail configurations also exist as the population evolves. T-tail configurations do well in the sonic-boom-loudness metric. This is because a T-tail configuration increases the effective length of the aircraft, leading to a reduced chance of rear shock coalescence, thus causing the sonic boom loudness to decrease. However, because of the increased weight and additional drag of T-tail designs, the range is severely penalized. The conventional tail configurations are slowly removed from the populations as the GA progresses. The Pareto front comprises only canard configurations.

To compare the effect of the type of horizontal stabilizer chosen on the objectives, an arbitrary geometry is chosen from the final population and the horizontal stabilizer type is changed, and the flight conditions and other geometry parameters are kept exactly the same. The rationale for doing this is to study the sensitivity of the objectives to the discrete configuration variables. Table 5 shows the results of the effect of interchanging the canard and T-tail. Because of the increased drag, the range of T-tail configuration is much reduced, compared with the canard configuration. The canard geometry causes additional compression in the front part of the pressure signature, which (after propagation through the atmosphere) leads to a stronger shock pressure rise in the sonic boom ground signature. The empty weight of the T-tail configuration is more than the canard configuration, and the drag is increased because of increased wetted area. This causes the T-tail geometry to have a higher thrust factor to takeoff in 7000 feet, which in turn causes the jet velocity to be higher than the canard configuration. Because of the off-axis presence of the T-tail, the sonic boom signature is spread over a longer duration than the signature produced by the canard design. This, combined with the fact that the canard configuration has a higher front-shock pressure rise, explains the increased loudness level of the canard configurations. Finally, to have static stability, the center of gravity should be located ahead of the neutral point. When compared with the canard geometry, the T-tail has the center of gravity shifted aft. Although the neutral point also shifts toward the rear sections, the shift is not as much, because the wing is the primary lift-producing component and it is unchanged. This explains the superiority of the canard configurations in the static stability objective.

From the foregoing explanation, it is clear that the T-tail configurations are superior to canard configurations with respect to sonic boom loudness. However, canard geometries are better at range, jet velocity, stability, and empty weight, among other things. An equally weighted optimizer attempts to minimize all the objectives at the same time, and canard geometries seem to be picked because of their superiority in more responses. However, if the sonic boom loudness is given more importance, it is possible that more T-tail geometries will be included in the GA populations.

B. Propulsion Cycle Tradeoffs

Figure 12 depicts the range versus sonic boom loudness plotted according to the propulsion cycle. It is apparent that the GA is biased toward FLADE cycles as the generation number increases. As in the previous case, the cycle is changed, keeping the flight conditions and the other geometry parameters exactly the same. To compare different propulsion cycles, the effective fan pressure ratio and overall pressure ratio of the different cycles are maintained the same. The effective fan pressure ratio of CDFS VCE is computed to be the product of the front fan pressure ratio and the fan pressure ratio of the core-driven-fan stage. The specific values are shown in Table 6.

Table 7 shows the effect of changing propulsion cycles on some of the objectives. After engine scaling, the empty weight of the aircraft increases from FLADE to MFTF to CDFS, thus total mission fuel increases from CDFS to MFTF to FLADE, because the gross weight is the same for all three cases. This helps explain the trend in mission range going from the highest using the FLADE to lowest using the CDFS. The cruise occurs at an optimum altitude for maximum range, with the stipulation that the rate of climb be at least 100 ft/s. In the case of the CDFS, because of the increased empty weight, the rate-of-climb limit is reached at a lower altitude than for the MFTF or FLADE. The lower altitude results in increased drag and also much more severe sonic boom loudness.

On the other hand, the MFTF cycle also seems to have an inferior performance in most responses, other than jet velocity, when compared with the FLADE cycle. To set the optimal thrust-to-weight ratio for each configuration, the thrust-to-weight ratio is parametrically varied to obtain an excess fuel capacity of no more than 15 lb. If all the thrust-to-weight-ratio values produce an excess fuel of more

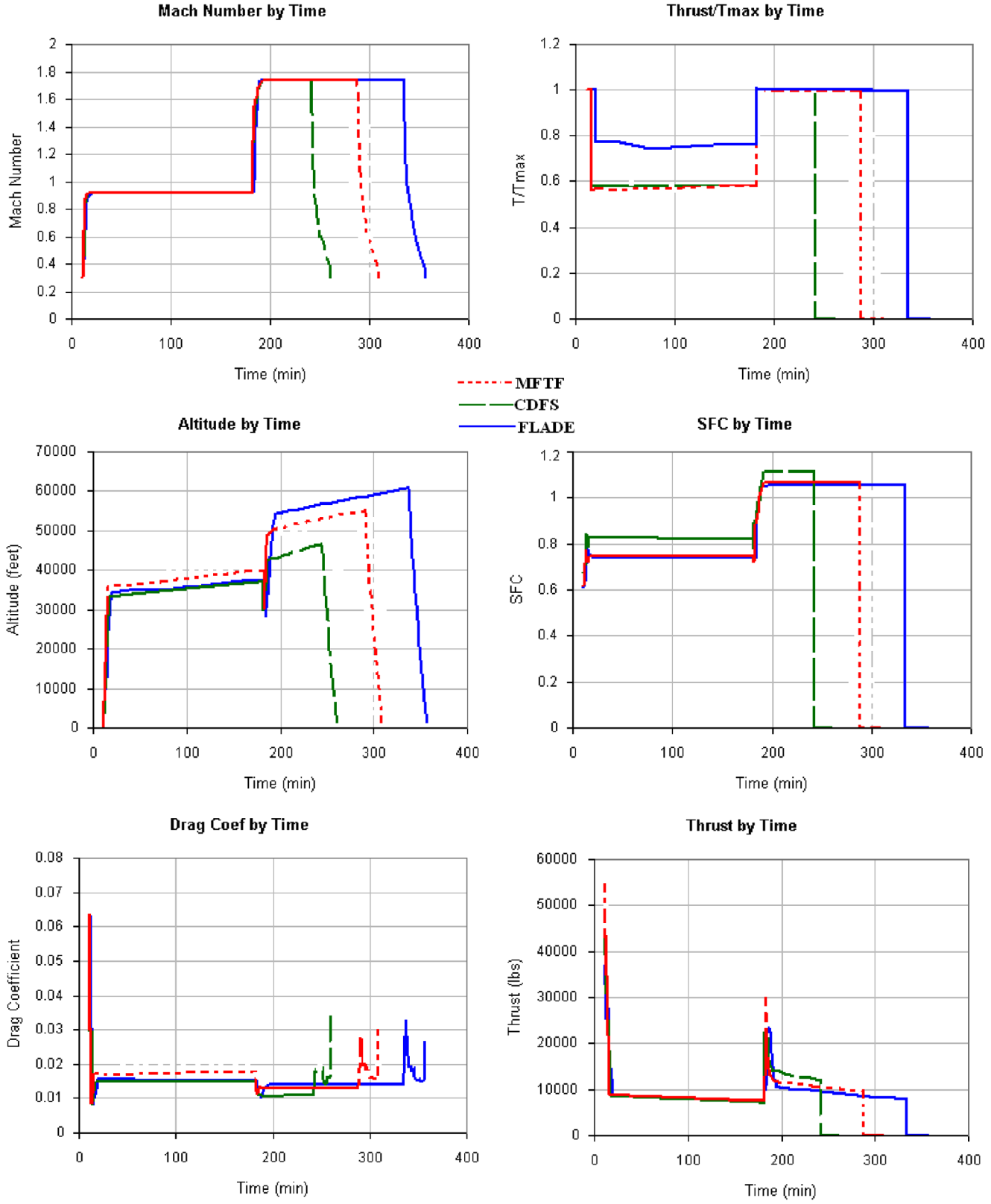

Fig. 14 Engine mission summary comparison.

than 15 lb, then the value corresponding to the largest range is chosen as the optimal thrust-to-weight ratio. In the current example, using the unscaled engine decks of MFTF and FLADE, the optimal TWR are determined to be 0.564 and 0.3857, with excess fuel capacity being 14505.2 and 11368.8 lb, respectively. The higher TWR for the MFTF causes the engine scale factor to be higher (0.6123) than with the FLADE (0.4384). Therefore, even though the unscaled engine weights are lower for MFTF, the scaled engine weight is lower for the FLADE cycle. With this information and the aforementioned reasons, it is not difficult to relate the responses shown in Table 7 to their respective cycles.

Figure 13a shows the performance of the different engine cycles in the jet velocity and range dimensions. The desired region in this figure is the upper left corner of the plot. The line represents a

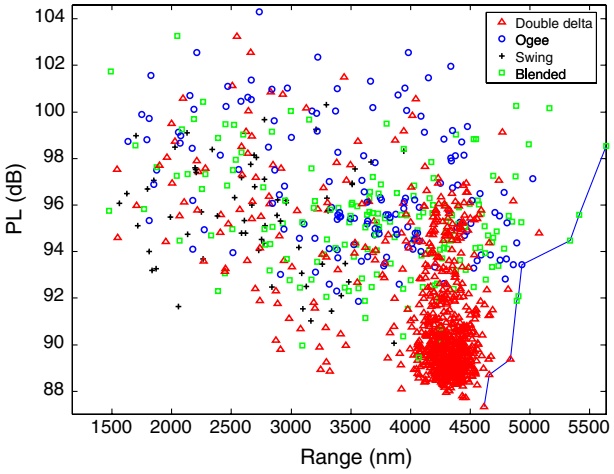

a) Range vs sonic boom loudness

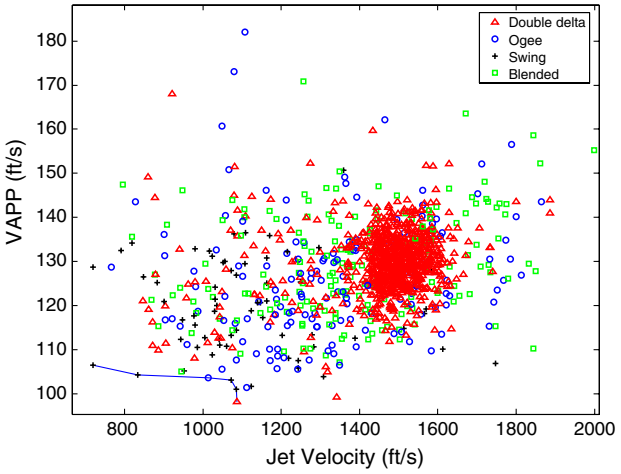

b) Jet velocity vs approach velocity

Fig. 15 Tradeoffs associated with wing topology.

Pareto-optimal line after GA termination. It is seen that MFTF designs occupy the lower-jet-velocity section of the Pareto front, and the FLADE designs cover the higher-range sections; the CDFS designs are inferior to both MFTF and FLADE in this two-dimensional plot. The FLADE cycle, by itself, is expected to have lower exit jet velocity than with the other two propulsion cycles. However, in the case considered here, the FLADE has the worst exit jet velocity. This is explained by Fig. 13b, which shows the exit velocity for each cycle type against the power setting. It is seen that FLADE consistently beats MFTF for any power setting. Interestingly, at a certain threshold, CDFS goes from being the worst-performing to the best-performing. Therefore, how well an engine cycle performs against the others depends on the engine sizing and how much thrust is required at take off (or, equivalently, the power setting). For the case under consideration, at the power setting used at takeoff (indicated by the markers), the FLADE has the worst jet velocity, even though it outperforms the other engines at that particular power setting.

Figure 14 shows the comparison of aircraft performance as a function of cycle type. For the CDFS design, in addition to having a heavier engine and thus less weight available for fuel, as mentioned above, the SFC-vs-time plot shows that the other cycles outperform the CDFS in fuel consumption for this design configuration. This is an additional reason why the CDFS design achieves such a poor range. In the supersonic regime, the altitude-vs-time plot verifies that the FLADE design flies at the highest altitude and (as mentioned before) incurs less drag. This fact is verified by examining the thrust-vs-time plot, which shows that the MFTF and CDFS designs have to operate at a higher thrust level to overcome the higher drag forces. This ends up lowering those design ranges by burning fuel more quickly than the FLADE design. The Mach number remains the same for each engine-cycle type. As expected, each engine cycle operates at maximum thrust in the supersonic portion of flight, which indicates that the engines are indeed sized correctly. However, in the subsonic portion, the MFTF and CDFS operate at a lower power setting than does the FLADE. The drag coefficient remains relatively similar for each engine cycle and varies only slightly, due to the altitude at which the concept vehicle is flying. Holding all other variables constant and varying only engine-cycle type shows that using the FLADE engine-cycle type produces the best overall system-level performance. This is additional evidence in support of

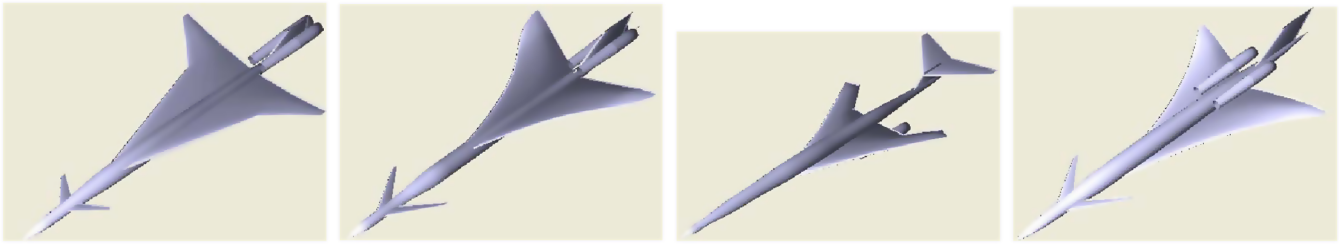

a) Double delta **b) Ogee** **c) Swing** **d) Blended**

Fig. 16 Wing topologies.

Table 8 Effect of wing planform on system responses

Variable	Double-delta	Ogee	Swing	Blended
Range, n mile	4493.1	3765.8	3925.5	4483.7
Jet velocity for 7000-ft takeoff, ft/s	1553.2	1367.4	1352.8	1563.8
Shock pressure rise, psf	0.352	1.13	0.385	0.358
Sonic boom, PL (dB)	88.48	99.66	91.22	90.61
Approach velocity, kt	124.3	117.1	112.1	134
Static stability penalty	0	4453.8	9184.9	2289.8
Empty weight, lb	42,194.2	45,114.3	44,460.1	41,690.5
Total fuel consumed	51,267.1	48,347.0	49,001.2	51,770.8
Engine scale factor	0.3891	0.4685	0.4288	0.3891
Cruise weight, lb	76,451	75,782	78,444	75,284
Cruise altitude, ft	52,092	54,519	49,707	51,523
Takeoff power setting	0.984	0.79	0.775	1

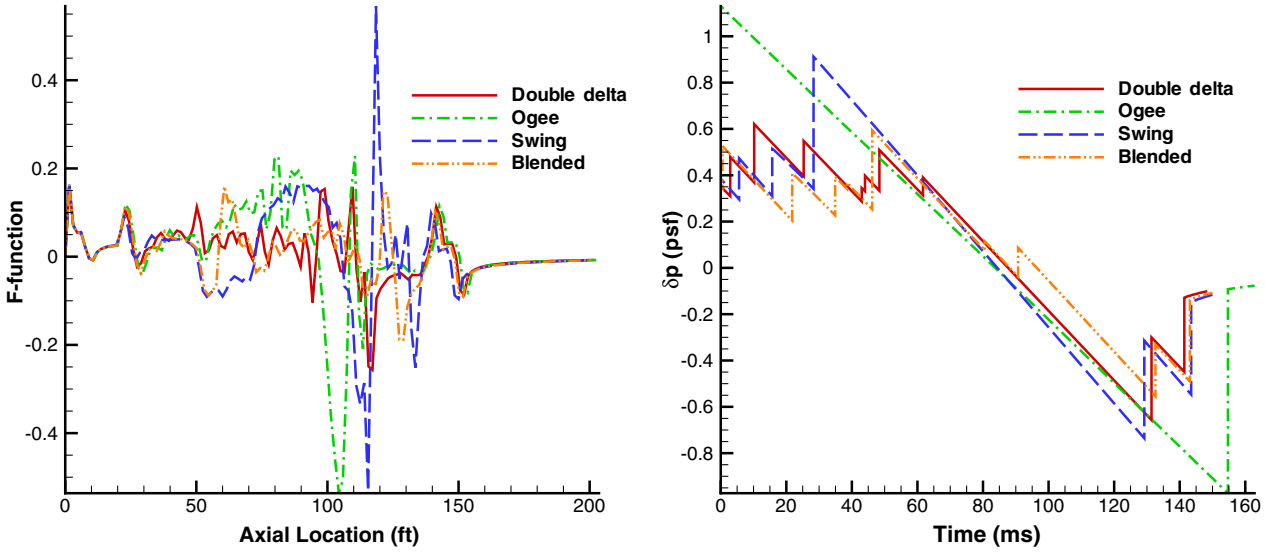

a) Near-field comparison

b) Ground signature comparison

Fig. 17 Effect of wing topology on sonic boom.

the previous hypothesis that any aircraft configuration has a better chance of performing well if it employs a FLADE engine cycle for its engine.

C. Wing Planform Tradeoffs

The choice of wing planform also has a major impact on the system-level responses. Figure 15a presents the comparison of the different wing planforms in the range-vs-sonic-boom-loudness plot. It is seen that the blended and double-delta planforms occupy the Pareto front in this plot, whereas the ogee- and swing-wing designs are slowly removed by the optimizer. In contrast, Fig. 15b presents the comparison of wing planforms in the jet-velocity-vs-approach-velocity space. In this plot, it is seen that swing-wing designs occupy the desired region of low approach velocity and low jet velocity. This is expected, because subsonically swept swing-wing designs have better low-speed performance.

Following the procedure presented in the canard and engine-cycle tradeoffs, the wing planform type is varied, keeping all other parameters constant. Figure 16 depicts the different wing topologies, for ready reference. Table 8 presents the results of this exercise. The ramp gross weight in all models is held constant. The optimal thrust to weight for double-delta, ogee, swing, and blended wings are computed to be 0.35, 0.4214, 0.3857, and 0.35, respectively. Because of the higher TWR, the engine scale factors for ogee- and swing-wing configurations are 0.4685 and 0.4288, respectively, compared with 0.3891 for the other two planform designs. This causes the empty weight of the ogee-wing configuration to be more than the swing-wing, double-delta, or blended-wing designs. The fuel available decreases in the same order. This explains the lower range for the ogee-wing designs. The swing-wing design also has lower range than with double-delta or blended-wing designs, due to inferior lift-to-drag ratios during cruise and lower total fuel available. Even though they are comparable in most objectives, the low-speed performance of the blended-wing design is inferior to the double-delta design.

The increased sonic boom loudness for the ogee wing can be explained as follows. Because of the shape of the ogee wing, there is a compression region throughout the length of the wing planform. Figure 17a compares the F-function of the configurations with varying wing planforms, and Fig. 17b shows the ground signatures of these wing designs. It is seen that the ogee-wing F-function has multiple wing shocks followed by a strong expansion and strong rear-wing shock. Because of the propagation mechanisms, the shocks ahead of the rear-wing expansion merge with the front-shock system, and the rear shocks merge to create a two-shock (N-wave) signature on the ground. This is known to produce an intense boom on the ground. The swing wing also has a steady compression region that causes the sonic boom ground signature to have a large shock overpressure. The double-delta wing, on the other hand, produces smaller-magnitude shocks separated by healthy expansion regions. This results in an almost-flat-top sonic boom signature for the double-delta design. The performance of the blended wing in the sonic boom objective is slightly more than the double-delta, due to the presence of additional shocks in the ground signature. This explains the preference of double-delta designs by the GA in the sonic boom response when all the other parameters are identical.

VI. Conclusions

A framework for concept selection of supersonic transport aircraft has been developed in this work through the use of advanced genetic algorithms and multiple contributing analyses. The conceptual design space exploration environment created here enables rapid search of possible concepts to determine the most promising based on requirements and physics-based analyses, not empirical relationships. Several important conceptual tradeoffs can be carried out using the multidisciplinary approach presented here. Because of the size of the design and objective space, these tradeoffs are inevitable. However, studying these and making an informed decision based on physics-based analyses is essential. Based on the assumptions made, the results of this study conclude that properly shaped double-delta wings with FLADE variable-cycle propulsion architecture and canard or T-tail configurations are best suited for further detailed study. The multidisciplinary aspect of the current work has the potential to arrive at a set of designs that can attempt to satisfy all these requirements simultaneously. Using the design framework developed as part of this study, updating requirements can be done simultaneously with vehicle design. This is very advantageous in the case of evolving requirements. Several extensions of this work are possible, the most obvious being enhancement of analysis tools, exploration of larger design spaces by including other geometry parameters (airfoil for example), inclusion of cost and complexity models, and assigning weighting factors to the objectives based on importance criteria. Furthermore, with proper analysis tools, the environment created in this study can be easily applied or extended to subsonic/supersonic/hypersonic or aircraft/rotorcraft conceptual analysis and design. Changing technology factors may also be introduced to allow aircraft design in the presence of uncertain technology impacts.

Appendix: Design Variables

Table A1 Design variables of interest and their ranges

Component	Alternatives	Parameter	Lower bound	Upper bound
Fuselage		Length	120	140
		Cabin location	0.25	0.4
		Cabin diameter	6.8	7.2
		Cabin length	30	50
		Diameter multipliers (×13)	0	1
		Nose droop factor	0	0.05
		Tail upsweep factor	0	1
Wing	Double-delta	Longitudinal apex location[a]	0.5	0.7
		Vertical location of wing plane	−0.85	0.5
		Aspect ratio	4	6
		Taper ratio	0.1	0.3
		Wing loading, psf	50	75
		Sweep, deg	40	65
		Dihedral (Root, Kink, tip), deg	0	10
		t/c (root)	0.022	0.035
		t/c (tip)	0.03	0.04
		Wing geometric twist at the kink, deg	0	2
		Wing geometric twist at the tip, deg	0	5
		Strake sweep, deg	70	78
	Ogee/blended	Longitudinal apex location[a]	0.5	0.7
		Vertical location of wing plane	−0.85	0.5
		Aspect ratio	1.8	2.2
		Taper ratio	0.02	0.08
		Wing loading, psf	50	70
		Glove aft sweep, deg	−30	0
		Dihedral (root, kink, tip), deg	0	10
		t/c (root)	0.025	0.04
		t/c (mid)	0.025	0.04
		t/c (tip)	0.02	0.03
		Wing geometric twist at the kink, deg	0	2
		Wing geometric twist at the tip, deg	0	5
		X1Mult (bezier control pt.)	0	1
		Y1Mult (bezier control pt.)	0	1
		X2Mult (bezier control pt.)	0	1
		Y2Mult (bezier control pt.)	0	1
	Swing	Longitudinal apex location[a]	0.5	0.7
		Vertical location of wing plane	−0.85	0.5
		Aspect ratio	3.5	5
		Taper ratio	0.45	0.65
		Wing loading, psf	60	90
		Subsonic sweep, deg	15	30
		Supersonic sweep, deg	60	72
		t/c (root)	0.12	0.14
		t/c (tip)	0.06	0.08
		Glove taper ratio	0.18	0.25
		Glove span multiplier	0.8	1.1
Horizontal tail	Canard	Longitudinal apex location[a]	0.1	0.2
		Aspect ratio	1.8	2.5
		Taper ratio	0.2	0.5
		Horizontal volume coefficient	0.1	0.16
		Sweep, deg	45	60
		t/c	0.03	0.05
	Conventional	Longitudinal apex location[a]	0.92	0.97
		Aspect ratio	1.6	2.2
		Taper ratio	0.1	0.3
		Horizontal volume coefficient	0.25	0.45
		Sweep, deg	45	60
		t/c	0.03	0.05
	T-tail	Location on vertical tail span[a]	0.9	0.96
		Aspect ratio	1.6	2.2
		Taper ratio	0.2	0.4
		Horizontal volume coefficient	0.25	0.35
		Sweep, deg	45	60
		t/c	0.03	0.05
Engine location	Under wing	Spanwise location of engine[a]	0.2	0.4
		Chordwise location of engine face	0.4	0.8
	Fuselage-mounted	Spanwise location of engine face[a]	0.7	0.85

(continued)

Table A1 Design variables of interest and their ranges (Continued)

Component	Alternatives	Parameter	Lower bound	Upper bound
Propulsion cycle	MFTF	Fan pressure ratio	1.8	3.26
		Overall pressure ratio	25.0	35.0
		Throttle ratio	1.0	1.1
		Extraction ratio	0.95	1.05
	CDFS VCE	Fan pressure ratio	1.6	2.0
		Overall pressure ratio	25	35
		Throttle ratio	1.0	1.1
		Extraction ratio	0.95	1.05
		CDFS pressure ratio	1.4	1.6
	FLADE VCE	Fan pressure ratio	1.8	3.26
		Overall pressure ratio	25	35
		Throttle ratio	1.0	1.1
		Extraction ratio	0.95	1.05
		FLADE bypass ratio	0.05	0.2
Flight conditions		Mach	1.6	1.8
		Gross weight	95,000	135,000

[a]Fraction of the characteristic length.

Acknowledgments

This work was supported in part by NASA Project NAS1-02117, titled "Decision Making Support for NASA's Aeronautics Research Mission Directorate," with Wu Li acting as technical monitor. The authors would like to acknowledge the help received from Russell Denney, Jason Kramer, Saam Ahmadi, and Jeff Varos of the Aerospace Systems Design Lab at Georgia Institute of Technology with the modeling and design of the propulsion cycle. The authors also acknowledge help received from Michael Buonanno.

References

[1] Darden, C. M., "The Importance of Sonic Boom Research in the Development of Future High Speed Aircraft," *Journal of the National Technical Association*, Vol. 65, No. 3, 1992, pp. 54–62.

[2] Henne, P. A., "Case for Small Supersonic Civil Aircraft," *Journal of Aircraft*, Vol. 42, No. 3, 2005, pp. 765–774.

[3] Morgenstern, J. M., "Tail-Braced Wing Aircraft and Configurations for Achieving Long Supersonic Range and Low Sonic Boom," Lockheed Martin Corp., Bethesda, MD, U.S. Patent No. 6729577, Issued May 2004.

[4] Henne, P., Howe, D., Wolz, R., and Hancock, J., "Supersonic Aircraft with Spike for Controlling and Reducing Sonic Boom," Gulfstream Aerospace Corp., Savannah, GA, U.S. Patent No. 6698684, Issued Mar. 2004.

[5] Tracy, R. R., Chase, J. D., and Kroo, I., "Tail-Braced Wing Aircraft and Configurations for Achieving Long Supersonic Range and Low Sonic Boom," Aerion Corp., Reno, NV, U.S. Patent No. 6857599, Issued Feb. 2005.

[6] McCurdy, D. A., "High Speed Research: 1994 Sonic Boom Workshop, Atmospheric Propagation and Acceptability Studies," NASA CP 3279, Oct. 1994.

[7] Baize, D. G., "NASA High Speed Research Program Sonic Boom Workshop," NASA CP 3335, Oct. 1995.

[8] Pawlowski, J. W., Graham, D. H., Boccadoro, C. H., Coen, P. G., and Maglieri, D. J., "Origins and Overview of the Shaped Sonic Boom Demonstration Program," AIAA Paper 2005-5, Jan. 2005.

[9] Wlezien, R., and Veitch, L., "The DARPA Quiet Supersonic Platform Program," AIAA Paper 2002-0143, Jan. 2002.

[10] McCullers, L. A., *Flight Optimization System, FLOPS. User's Guide, Release 6.13*, Vigyan, Inc., Hampton, VA, May 2005.

[11] Evans, A., L., Follen, G., Naiman, C., and Lopez, I., "Numerical Propulsion System Simulation's National Cycle Program," AIAA Paper 1998-3113, July 1998.

[12] Rallabhandi, S. K., and Mavris, D. N., "Aircraft Geometry Design and Optimization for Sonic Boom Reduction," *Journal of Aircraft*, Vol. 44, No. 1, 2007, pp. 35–47. doi:10.2514/1.20456

[13] Gloudemans, J. R., Davis, P. C., and Gelhausen, P. A., "A Rapid Geometry Modeler for Conceptual Aircraft," AIAA Paper 1996-52, Jan. 1996.

[14] Berton, J., Haller, W., Senick, P., Jones, S., and Seidel, J., "A Comparative Propulsion System Analysis for the High-Speed Civil Transport," NASA TM-2005-213414, Feb. 2005.

[15] Salay, C., and Elliot, D., "Matching Engine and Aircraft Lapse Rates for High Speed Civil Aircraft," *Journal of Aircraft*, Vol. 33, No. 1, 1996, pp. 61–67.

[16] Carey, J. P., Lee, R., and Majjigi, R. K., "Acoustically Shielded Exhaust System for High Thrust Jet Engines," General Electric Co., Schenectady, NY, U.S. Patent No. 5402963, Issued Apr. 1995.

[17] Harris, R. V., "An Analysis and Correlation of Aircraft Wave Drag," NASA TM X-947, Apr. 1964.

[18] Carlson, H., Chu, J., Ozoroski, L., and Mccullers, A., "Guide to AERO2S and WINGDES Computer Codes for Prediction and Minimization of Drag Due to Lift," NASA TP 3637, Nov. 1997.

[19] Middleton, W. D., and Lundry, J. L., "A System of Aerodynamic Design and Analysis of Supersonic Aircraft," NASA CR 3351, Dec. 1980.

[20] Raymer, D. P., *Aircraft Design: A Conceptual Approach*, AIAA, Reston, VA, 1999.

[21] Coen, P. G., "Development of a Computer Technique for the Prediction of Transport Aircraft Flight Profile Sonic Boom Signatures," M.S. Thesis, George Washington Univ., Washington, DC, Mar. 1983.

[22] Plotkin, K. J., "PCBoom3 Sonic Boom Prediction Model—Version 1.0c," Wyle Research Labs., Rept. AFRL-HE-WP-TR-2001-0155, Arlington, VA, May 1996.

[23] Needleman, K. E., Darden, C. M., and Mack, R. J., "A Study of Loudness as a Metric for Sonic Boom Acceptability," AIAA Paper 91-0496, June 1991.

[24] Stone, S. C., Henderson, J. L., Nazari, M. M., Boyd, W. N., Becker, B. T., Bhatia, K. G., Giles, G. L., and Wrenn, G. A., "Evaluation of Equivalent Laminated Plate Solution (ELAPS) in HSCT Sizing," AIAA Paper 2000-1452, Apr. 2000.

[25] Onat, E., and Klees, G. W., "A Method to Estimate Weight and Dimensions of Large and Small Gas Turbine Engines," NASA CR 159481, Jan. 1979.

[26] Tong, M. T., Ghosn, L. J., and Halliwell, I., "A Computer Code for Gas Turbine Engine Weight and Disk Life Estimation," American Society for Mechanical Engineers, Paper GT-2002-30500, 2002.

[27] Zitzler, E., Laumanns, M., and Thiele, L., "SPEA2: Improving the Strength Pareto Evolutionary Algorithm," *Computer Engineering and Networks Laboratory (TIK)*, Dept. of Electrical Engineering, ETH Zürich, Rept. 103, Sept. 2001.

[28] Khare, V., "Performance Scaling of Multi-Objective Evolutionary Algorithms," M.S. Thesis, Univ. of Birmingham, Birmingham, England, U.K., 2002.

[29] Deb, K., *Multi-Objective Optimization using Evolutionary Algorithms*, Wiley, New York, 2002.

[30] Ignizio, J., *Goal Programming and Extensions*, Lexington Books, Lanham, MD, 1976.

[31] Parmee, I., "Genetic Algorithms and Hydropower System Design," *Computer-Aided Civil and Infrastructure Engineering*, Vol. 13, No. 1, Jan. 1998, pp. 31–41. doi:10.1111/0885-9507.00083

[32] Eshelman, L., and Schaffer, J., "Real Coded Genetic Algorithms and Interval Schemata," *Foundations of Genetic Algorithms*, Vol. 2, Morgan Kaufmann, San Mateo, CA, 1993, pp. 187–202.

[33] Deb, K., "Simulated Binary Crossover for Continuous Search Space," *Complex Systems*, Vol. 9, No. 2, 1995, pp. 115–148.

[34] Deb, K., and Beyer, H. G., "Self-Adaptation in Real-Parameter Genetic

Algorithms with Simulated Binary Crossover," *Proceedings of Genetic and Evolutionary Computation Conference*, Morgan Kaufmann, San Mateo, CA,1999, pp. 172–179.

[35] Ballester, J. P., and Carter, J. N., "Real-Parameter Genetic Algorithms for Finding Multiple Optimal Solutions in Multi-Modal Optimization," *Proceedings of the Genetic and Evolutionary Computation Conference*, Lecture Notes in Computer Science, Springer, New York, 2003, pp. 706–717.

[36] Buonanno, M. A., "A Method for Aircraft Concept Exploration Using Multicriteria Interactive Genetic Algorithms," Ph.D. Thesis, School of Aerospace Engineering, Georgia Inst. of Technology, Atlanta, GA, Dec. 2005.

[37] Harik, G. R., "Finding Multimodal Solutions Using Restricted Tournament Selection," *Proceedings of the Sixth International Conference on Genetic Algorithms*, Morgan Kaufmann, San Mateo, CA, 1995, pp. 24–31.

[38] Ishibuchi, H., and Shibata, Y., "An Empirical Study on the Effect of Mating Restriction on the Searchability of EMO Algorithms," *Evolutionary Multi-Criterion Optimization*, Springer, New York, 2003, pp. 433–447.

[39] Eby, D., Averill, R. C., Gelfand, B., Punch, W. F., Mathews, O., and Goodman, E. D., "An Injection Island GA for Flywheel Design Optimization," *Eufit '97: 5th European Congress on Intelligent Techniques and Soft Computing*, edited by H. J. Zimmerman, European Lab. for Intelligent Techniques Engineering Foundation (ELITE), Aachen, Germany, Sept. 1997, pp. 687–691.

[40] Thain, D., Tannenbaum, T., and Livny, M., "Condor and the Grid," *Grid Computing: Making the Global Infrastructure a Reality*, edited by F. Berman, G. Fox, and T. Hey, Wiley, New York, Dec. 2002.

[41] Thain, D., Tannenbaum, T., and Livny, M., "Distributed Computing in Practice: The CONDOR Experience," *Concurrency, Practice and Experience*, Vol. 17, Nos. 2–4, 2005, pp. 323–356. doi:10.1002/cpe.938

[42] Fenbert, J., Ozoroski, L., Geiselhart, K., Shields, W., and McElroy, M., "Concept Development of a Mach 2.4 High-Speed Civil Transport," NASA TP-1999-209694, Dec. 1999.